JACS
JOURNAL OF THE AMERICAN CHEMICAL SOCIETY
pubs.acs.org/JACS
Article

Temperature Cycling Enables Efficient ^{13}C SABRE-SHEATH Hyperpolarization and Imaging of [1-^{13}C]-Pyruvate

Patrick TomHon,* Mustapha Abdulmojeed, Isaiah Adelabu, Shiraz Nantogma, Mohammad Shah Hafez Kabir, Sören Lehmkuhl, Eduard Y. Chekmenev, and Thomas Theis*

Cite This: J. Am. Chem. Soc. 2022, 144, 282−287
Read Online

ABSTRACT: Molecular metabolic imaging in humans is dominated by positron emission tomography (PET). An emerging nonionizing alternative is hyperpolarized MRI of ^{13}C-pyruvate, which is innocuous and has a central role in metabolism. However, similar to PET, hyperpolarized MRI with dissolution dynamic nuclear polarization (d-DNP) is complex costly, and requires significant infrastructure. In contrast, Signal Amplification By Reversible Exchange (SABRE) is a fast, cheap, and scalable hyperpolarization technique. SABRE in SHield Enables Alignment Transfer to Heteronuclei (SABRE-SHEATH) can transfer polarization from parahydrogen to ^{13}C in pyruvate; however, polarization levels remained low relative to d-DNP (1.7% with SABRE-SHEATH versus ≈60% with DNP). Here we introduce a temperature cycling method for SABRE-SHEATH that enables >10% polarization on [1-^{13}C]-pyruvate, sufficient for successful *in vivo* experiments. First, at lower temperatures, ≈20% polarization is accumulated on SABRE catalyst-bound pyruvate, which is released into free pyruvate at elevated temperatures. A kinetic model of differential equations is developed that explains this effect and characterizes critical relaxation and buildup parameters. With the large polarization, we demonstrate the first ^{13}C pyruvate images with a cryogen-free MRI system operated at 1.5 T, illustrating that inexpensive hyperpolarization methods can be combined with low-cost MRI systems to obtain a broadly available, yet highly sensitive metabolic imaging platform.

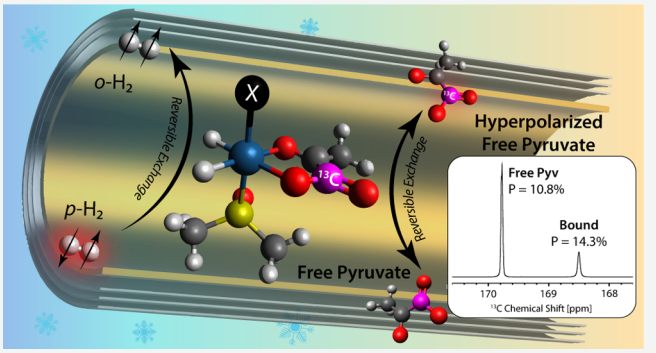

INTRODUCTION

Hyperpolarized magnetic resonance imaging (MRI) is emerging as a technique to track biomolecular metabolism without radioactive labels or ionizing radiation.[1] Hyperpolarized (HP) MRI is currently under investigation in clinical trials to gain insights and diagnose metabolic disease states such as cancer,[1] diabetes,[2] or cardiovascular disease.[3,4] HP pyruvate is a leading candidate as a metabolic marker due to its safety and its central role in metabolism.[1] Through measuring pyruvate metabolism, striking advancements have been made in the detection of cancer cells in prostate,[5,6] breast,[7] and brain[8] tissues.[9] However, the leading method to hyperpolarize pyruvate, dissolution dynamic nuclear polarization (d-DNP), is limited in broad availability due to its high cost (≈$2.5M), long contrast agent production times (≈30 min or more), and instrument complexity.[10,11] In contrast, Signal Amplification By Reversible Exchange (SABRE)[12] is a fast (≈20 s), cheap (≈$25,000), and scalable hyperpolarization technique using parahydrogen (p-H_2) as a source of spin order to directly hyperpolarize small molecules in solutions, including pyruvate.[12−15]

The hyperpolarization of heteronuclei (*e.g.*, ^{13}C) is optimized in magnetic shields that establish microtesla magnetic fields, called SABRE in Shield Enables Alignment Transfer to Heteronuclei (SABRE-SHEATH).[16−18] Previous work has demonstrated ^{13}C pyruvate hyperpolarization with SABRE-SHEATH, but it remained limited in polarization relative to the high values of DNP (1.7% vs ≈60%).[13,14] Here, we present a combination of advances including the use of temperature cycling to overcome the *in vivo* polarization threshold of 10% with SABRE-SHEATH. The results of this study also indicate that further optimization is possible to maximize the critical molar polarization, defined as the product of concentration and polarization (introduced by Shchepin et al.[19] and Knecht et al.[20]), ultimately the most important hyperpolarization parameter required for *in vivo* translation.[5,11,21]

Previous demonstrations of parahydrogen induced polarization with side arm hydrogenation (PHIP-SAH) on pyruvate

Received: September 13, 2021
Published: December 23, 2021

https://doi.org/10.1021/jacs.1c09581
J. Am. Chem. Soc. 2022, 144, 282−287

have shown the feasibility of *in vivo* studies.[22,23] These experiments demonstrate that an initial ^{13}C polarization of 10%, which was purified to give a 35 mM 3.5% polarization solution at the time of injection, is sufficient for *in vivo* chemical shift MRI.[22] PHIP-SAH involves synthesis of a propargyl pyruvate precursor, hydrogenation, complex spin transfer, hydrolysis, and phase transfer steps to obtain HP pyruvate.[22] In contrast, the facile nature of SABRE enables direct hyperpolarization of the ^{13}C spins in pyruvate with reduced complexity. Figure 1 highlights the catalytically active

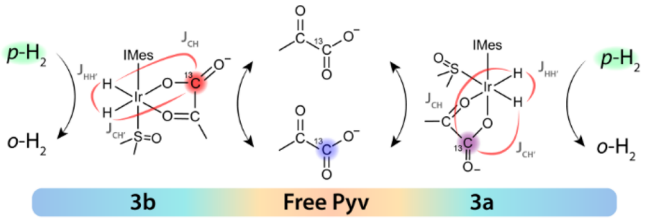

Figure 1. Hyperpolarization scheme of [1-^{13}C]-pyruvate, with a gradient representation of temperature cycling. The full IMes ligand is omitted for diagram clarity, where IMes = 1,3-bis(2,4,6-trimethylphenyl)imidazole-2-ylidene.

species originally described by Iali et al., where optimized hyperpolarization levels of [1-^{13}C]-pyruvate reached 0.96%,[13] substantially below the ^{13}C polarization achieved with DNP[6] or the PHIP-SAH methods.[22,24]

In the present work, we highlight that sufficiently fast p-H_2 exchange still occurs in the complex at low temperatures to efficiently polarize bound pyruvate. Using this feature, we implement time-dependent temperature gradients with SABRE-SHEATH on [1-^{13}C]-pyruvate to reach $P_{^{13}C}$ (^{13}C polarization) of 10.8% on free pyruvate in solution, which is over 6 times greater than previous optimized results (Figure 2A). Additionally, this figure is on par with the initial polarization achieved on allyl pyruvate with SAH-PHIP,[22] indicating that with simple purification methods[20,24] a viable biocompatible injectable for *in vivo* imaging could be produced. This is enabled by starting with $P_{^{13}C} \approx 20\%$ on catalyst-bound pyruvate at lower temperatures. We also provide detailed insights and a kinetic model to describe exchange dynamics and relaxation processes during temperature gradients, which modulate substrate and hydride exchange rates. As detailed below, further optimization yields even greater molar polarization levels (concentration × %*P*) as needed for *in vivo* studies.[9,20,22]

RESULTS AND DISCUSSION

The spectrum and results shown in Figure 2A are the maximum achieved single-shot polarization. These data show 14.3% polarization on bound pyruvate (after warm-up) and 10.8% on free pyruvate, corresponding to a total polarization of 11.8%. The calculation of %*P* uses the reference signal displayed in Figure 2B and is detailed in the Supporting Information. This result is enabled by (a) the use of a high catalyst to substrate ratio (5 equiv of pyruvate, 3.3 equiv of DMSO), as done in previous work;[14,25] (b) the use of [1-^{13}C]-pyruvate (both [2-^{13}C]-pyruvate and [1,2-$^{13}C_2$]-pyruvate give lower polarizations under identical conditions); and (c) precooling to slow exchange followed by bubbling at elevated temperature causing a time-dependent temperature gradient. To ensure reproducibility, we conducted the same experiment five times on different days and obtained an average of 10 ± 1% polarization on free pyruvate (see the Supporting Information). On bound pyruvate, polarization levels approaching 20% are observed when bubbling at even lower temperatures as detailed below.

Using the high polarization on [1-^{13}C]pyruvate, we acquired a ^{13}C image, shown in Figure 2C, utilizing a fast spin echo sequence at 1.5 T of a cryogen-free MRI system that can be operated at any field between 5 mT and 3 T. At the clinically relevant field of 1.5 T, we imaged the sample directly in an NMR tube with submillimeter resolution. The HP signal enables 3D multislice ^{13}C-imaging of the 3.45 mm cross-sectional area of the NMR tube (full details are provided in the Supporting Information). As can be seen in the images, even

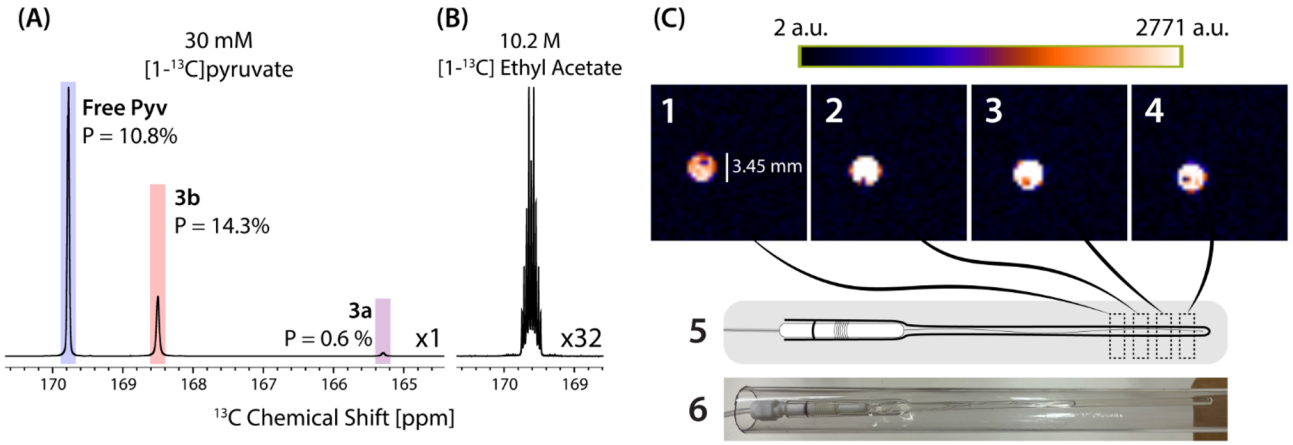

Figure 2. (A) NMR spectrum of hyperpolarized [1-^{13}C]-pyruvate in free and catalyst-bound forms. This spectrum was acquired with a sample of 30 mM [1-^{13}C]-pyruvate, 20 mM DMSO, and 6 mM IMes catalyst in CD_3OD. (B) Thermal reference spectrum of [1-^{13}C]-ethyl acetate at 9.4 T, used for calculation of the polarization. (C) MRI of HP [1-^{13}C]-pyruvate sample of 60 mM [1-^{13}C]-pyruvate, 40 mM DMSO, and 12 mM IMes catalyst in CH_3OH. Four axial slices of the image are taken in 1−4, with the NMR tube phantom and corresponding slice positioning shown in 5 and 6. The images are acquired with a fast spin echo sequence at 1.5 T with 64 × 64 voxels, 30 × 30 mm^2 field of view, a single echo train with 64 lines, and an overall acquisition time of 1.5 s. Full details regarding the setup and sequence are in the Supporting Information. The polarization obtained in the MRI was 5.85% by comparison to a thermal phantom.

https://doi.org/10.1021/jacs.1c09581
J. Am. Chem. Soc. 2022, 144, 282−287

the small, submillimeter sized capillary can be resolved in the images.

To characterize the temperature dependence of the hyperpolarization, we conducted the experiments depicted in Figure 3A–E. We used a pneumatic shuttle,[26] where the sample is first cooled in the probe and subsequently shuttled out of the cooled atmosphere into magnetic shields for SABRE-SHEATH.[13,27,28] Figure 3E shows the change in sample temperature as a function of bubbling time when starting at a sample temperature of 0 °C. The temperature was assessed with an internal methanol thermometer (see Supporting Information).

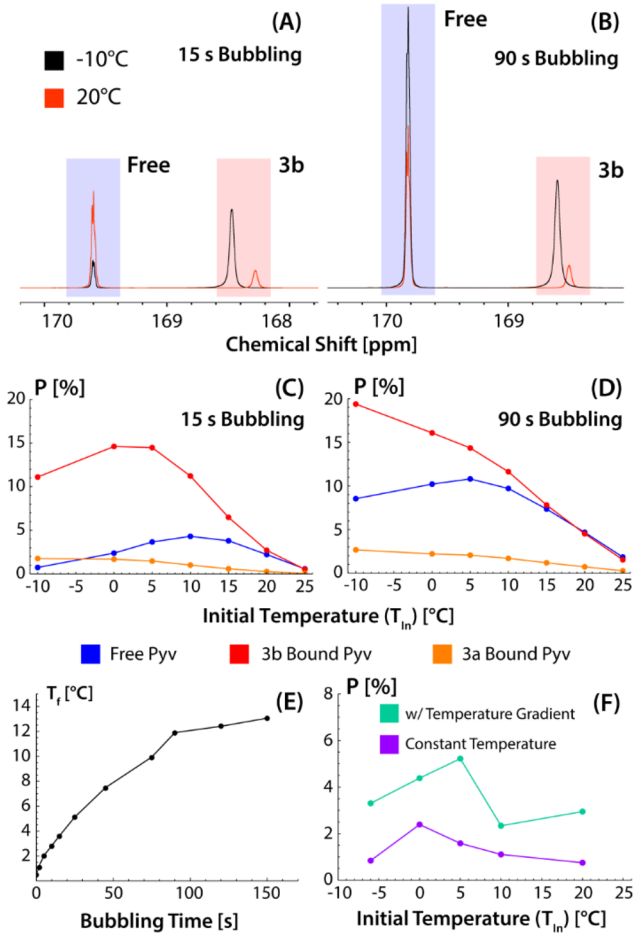

Figure 3. Variable temperature comparisons in the hyperpolarization of [1-^{13}C]-pyruvate. (A, B) Comparison of HP spectra obtained with initial sample temperatures of −10 and 20 °C using (A) 15 s bubbling and (B) 90 s bubbling. (C, D) Comparison of temperature dependence of [1-^{13}C]-pyruvate hyperpolarization with (C) 15 s bubbling and (D) 90 s bubbling. (E) Final sample temperature with variable bubbling time for an initial sample temperature of 0 °C in the pneumatic shuttling setup. (F) Comparison of polarization obtained on free pyruvate with and without a temperature gradient using manual sample transfer.

At low initial temperature, the slower exchange promotes efficient polarization buildup on the catalyst-bound pyruvate. This effect is evidenced by up to 20% polarization on the catalyst-bound pyruvate achieved by starting at the lowest temperature of −10 °C (see Figure 3C). With only 15 s of bubbling (Figure 3B), the polarization remains almost exclusively on the bound species **3b**. In contrast to previous work,[14] our data suggest that, at low temperatures, efficient hydrogen exchange still occurs on **3b** and **3a** species, yet at a sufficiently slow rate to allow the weak hydride−^{13}C couplings to pump large degrees of polarization onto bound ^{13}C pyruvate, which barely exchanges. As the sample warms during the bubbling period, [1-^{13}C]-pyruvate can exchange off the catalyst more rapidly while SABRE continues, albeit with reduced efficiency, ultimately leading to high polarization on free pyruvate. As is evident from Figure 3B,C, at even further elevated temperatures the free and bound polarization numbers equilibrate due to efficiently exchanging polarization pools. To unequivocally confirm that experiments with a temperature gradient give higher polarization than experiments with constant temperature, we conducted the study shown in Figure 3F. For this direct comparison, we had to use manual sample transfer experiments with a 1.1 T benchtop NMR spectrometer. In these experiments, the sample is either bubbled in a water bath at constant temperature in a magnetic shield (purple, Figure 3F) or first precooled in a water bath at a set temperature and then bubbled in the shield at ambient temperature (green, Figure 3F). The constant temperature experiments consistently stay below the experiments with temperature gradients: lower relative polarization values in these data, compared to automated shuttling, are due to unavoidable inconsistencies in slow manual sample transfer. Additionally, the temperature gradient experienced in this setup is different from that in shuttling experiments. In the shuttling system, the sample is bubbled in an atmosphere at ≈14 °C (see Figure 3E), while in the manual transfer experiments the sample is just moved into a room temperature (≈23 °C) atmosphere.

Relaxation and polarization buildup data shown in Figure 4 additionally support and characterize the described dynamics.

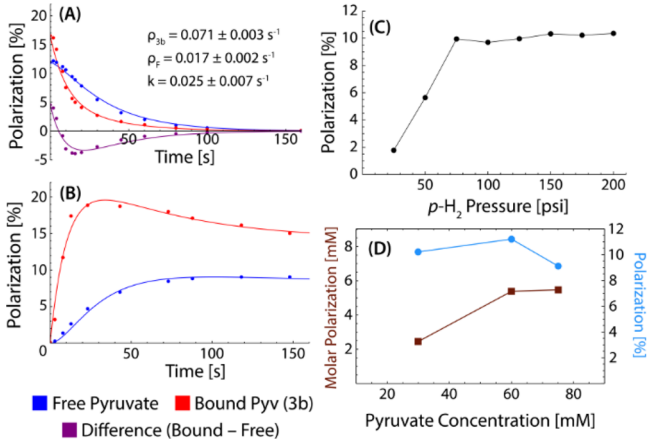

Figure 4. Relaxation, buildup, pressure, and concentration dependence. (A) Low-field (0.3 μT) relaxation and (B) polarization buildup data for free and bound pyruvate. Relaxation data are acquired after p-H_2 bubbling is stopped followed by a variable delay, while buildup data are acquired with variable bubbling periods. The data are fit to curves derived from the discussed differential equations (eqs 1–5). Since the resulting analytical solutions are lengthy, they are integrated and detailed in the Supporting Information. Table S5 gives all fit parameters. In (A) the temperature is constant and approximately 14 °C. (C) Pressure dependence of pyruvate polarization. (D) Sample concentration dependence for pyruvate polarization and molar polarization. Catalyst and DMSO concentrations are scaled at constant ratio. All data are acquired at an initial sample temperature of 0 °C.

https://doi.org/10.1021/jacs.1c09581
J. Am. Chem. Soc. 2022, 144, 282−287

We fit the data to a two-state (bound−free) model, which we developed inspired by previous work.[29] First, for relaxation dynamics in the absence of a pumping term (Figure 4A), the model takes into account chemical exchange and relaxation of the bound and free pyruvate species.

$$\frac{dP_B}{dt} = -(k + \rho_B)P_B[t] + kP_F[t] \quad (1)$$

$$\frac{dP_F}{dt} = kP_B[t] - (k + \rho_F)P_F[t] \quad (2)$$

Here P_B and P_F are the free and bound polarizations, k is the pyruvate exchange rate, and ρ_B and ρ_F are the relaxation rates of the free and bound pyruvate species. Solving the system of differential equations yields a fitting function for the bound and free spin relaxations. The full derivation of the fitting functions is given in the Supporting Information.

After solving these differential equations, we use the resulting model to fit the relaxation data in Figure 4A. At t = 0 the bound polarization exceeds the free polarization. The difference of the two is illustrated by the purple curve in Figure 4A. Initially, bound polarization decreases quickly because of exchange and relaxation. In contrast, the free polarization only experiences a very slow initial decrease because of the exchange with the highly polarized bound species. After about 8 s, the free polarization surpasses the bound polarization due to faster relaxation of the bound species.

A similar model is used to fit the polarization buildup data displayed in Figure 4B. The only difference is that we introduce a temperature (*i.e.*, bubbling time) dependent polarization pumping rate, Γ,

$$\frac{dP_B}{dt} = \Gamma - (k + \rho_B)P_B[t] + kP_F[t] \quad (3)$$

$$\frac{dP_F}{dt} = kP_B[t] - (k + \rho_F)P_F[t] \quad (4)$$

$$\Gamma = b + ae^{-t/\tau} \quad (5)$$

where eq 4 is identical to eq 2. The present model for Γ is purely empirical with fit parameters b, a, and τ. After this new set of differential equations is solved, only k, b, a, and τ are used as fit parameters. ρ_B and ρ_F are used as extracted from the relaxation data (see the Supporting Information for details). With this model, the fits explain the rapid initial buildup of bound polarization where pumping is efficient yet pyruvate exchange is inefficient. We point out that, without a temperature-dependent pumping rate Γ, the resulting models cannot represent the data in any reasonable way even if a temperature-dependent k is used. It appears that Γ has a larger temperature dependence than the pyruvate exchange k. In forthcoming work, we will examine this question and characterize the activation parameters of both hydrogen and pyruvate exchange in full. In the current absence of activation enthalpy and entropy and without knowledge of the exact J-coupling values that drive polarization transfer from p-H_2 to bound [1-^{13}C]-pyruvate, the empirical model for Γ gives valuable information, showing that hydrogen exchange becomes too fast at elevated temperatures to effectively drive SABRE. Therefore, temperature cycling solves the conundrum of having to optimize both hydrogen exchange and substrate exchange simultaneously.

Finally, in Figure 4C we illustrate that p-H_2 is not the limiting substrate at pressures above 75 psi for the investigated sample composition of 6 mM Ir-IMes catalyst, 20 mM DMSO, and 30 mM [1-^{13}C]-pyruvate. This graph implies that at higher substrate and catalyst concentrations the p-H_2 pressure can be increased to maintain the same polarization levels while boosting the ultimately important molar polarization. This insight is further stressed by the results displayed in Figure 4D, which demonstrate the scalability of ^{13}C pyruvate polarization from 30 mM [1-^{13}C]-pyruvate (where all the previously discussed results were obtained) to 60 mM [1-^{13}C]-pyruvate (maintaining the same ratios of catalyst and DMSO). Doubling of the concentration actually leads to an increase in polarization, more than doubling the molar polarization, indicating that 60 mM [1-^{13}C]-pyruvate may be the ideal concentration for future studies. Shifting to an even higher concentration yielded slightly reduced polarization; however, these higher concentrated samples are likely to be para-hydrogen limited (see Figure 4C), so higher p-H_2 pressures may return similar polarization levels while boosting molar polarization.

CONCLUSION

In summary, we demonstrated a high (11.8% weighted average) total polarization for [1-^{13}C]-pyruvate and 10.8% free polarization, paving the way for further optimization and significantly enhancing the feasibility of *in vivo* work. Specifically, the facile and robust nature of SABRE hyperpolarization relative to other hyperpolarization methods makes it an easily scalable technology. In these results, we emphasize the role that spin system, sample composition, and temperature gradients play in achieving high polarization levels. A kinetic model of differential equations was used to rationalize the high polarization levels. We used these high polarization levels to acquire multislice HP ^{13}C images with a cryogen-free MRI system operated at 1.5 T. This achievement indicates that it is possible to combine low-cost hyperpolarization with low-cost MRI to achieve high-sensitivity molecular imaging. Future work will focus on partnering these methods with previous demonstrations of catalyst extraction[30] or phase switching[31] to achieve safely injectable solutions for *in vivo* demonstrations at the preclinical level, driving this technology toward clinical applications.

ASSOCIATED CONTENT

Supporting Information

The Supporting Information is available free of charge at https://pubs.acs.org/doi/10.1021/jacs.1c09581.

Additional figures and results, including polarization calculations and fitting parameters, as discussed in the text (PDF)

AUTHOR INFORMATION

Corresponding Authors

Patrick TomHon − *Department of Chemistry, North Carolina State University, Raleigh, North Carolina 27606, United States;* orcid.org/0000-0003-3202-9812; Email: pmtomhon@ncsu.edu

Thomas Theis − *Department of Chemistry and Department of Physics, North Carolina State University, Raleigh, North Carolina 27606, United States; Joint Department of Biomedical Engineering, University of North Carolina,*

https://doi.org/10.1021/jacs.1c09581
J. Am. Chem. Soc. 2022, 144, 282−287

Chapel Hill, and North Carolina State University, Raleigh, North Carolina 27606, United States; orcid.org/0000-0001-6779-9978; Email: ttheis@ncsu.edu

Authors

Mustapha Abdulmojeed − *Department of Chemistry, North Carolina State University, Raleigh, North Carolina 27606, United States*

Isaiah Adelabu − *Department of Chemistry, Wayne State University, Detroit, Michigan 48202, United States*

Shiraz Nantogma − *Department of Chemistry, Wayne State University, Detroit, Michigan 48202, United States*

Mohammad Shah Hafez Kabir − *Department of Chemistry, Wayne State University, Detroit, Michigan 48202, United States*

Sören Lehmkuhl − *Department of Chemistry, North Carolina State University, Raleigh, North Carolina 27606, United States*

Eduard Y. Chekmenev − *Department of Chemistry, Wayne State University, Detroit, Michigan 48202, United States; Integrative Biosciences (Ibio), Wayne State University, Karmanos Cancer Institute (KCI), Detroit, Michigan 48202, United States; Russian Academy of Sciences, 119991 Moscow, Russia;* orcid.org/0000-0002-8745-8801

Complete contact information is available at: https://pubs.acs.org/10.1021/jacs.1c09581

Notes

The authors declare the following competing financial interest(s): Thomas Theis holds stock in Vizma Life Sciences LLC (VLS) and is President of VLS. VLS is developing products related to the research being reported. The terms of this arrangement have been reviewed and approved by NC State University in accordance with its policy on objectivity in research. The authors have filed a provisional patent application through NC State University with the USPTO regarding this work (Application# 63/203,591). EYC discloses a stake of ownership in XeUS Technologies, LTD.

■ ACKNOWLEDGMENTS

Research reported in this publication was supported by the National Institute of Biomedical Imaging and Bioengineering of the National Institutes of Health under Award Nos. NIH R21EB025313 and NIH R01EB029829. The content is solely the responsibility of the authors and does not necessarily represent the official views of the National Institutes of Health. In addition, we acknowledge funding from the Mallinckrodt Foundation, the National Science Foundation under Award No. NSF CHE-1904780, from the National Cancer Institute under Award No. NCI 1R21CA220137, and from the North Carolina Biotechnology Center in the form of a Translational Research Grant. Finally, we would like to acknowledge the support from NCSU's METRIC providing access to NMR instrumentation.

■ REFERENCES

(1) Serrao, E. M.; Brindle, K. M. Potential Clinical Roles for Metabolic Imaging with Hyperpolarized [1-^{13}C]Pyruvate. *Front. Oncol.* **2016**, *6*, 59.

(2) Rider, O. J.; Apps, A.; Miller, J. J. J. J.; Lau, J. Y. C.; Lewis, A. J. M.; Peterzan, M. A.; Dodd, M. S.; Lau, A. Z.; Trumper, C.; Gallagher, F. A.; Grist, J. T.; Brindle, K. M.; Neubauer, S.; Tyler, D. J. Noninvasive in Vivo Assessment of Cardiac Metabolism in the Healthy and Diabetic Human Heart Using Hyperpolarized ^{13}C MRI. *Circ. Res.* **2020**, *126*, 725−736.

(3) Cunningham, C. H.; Lau, J. Y. C.; Chen, A. P.; Geraghty, B. J.; Perks, W. J.; Roifman, I.; Wright, G. A.; Connelly, K. A. Hyperpolarized ^{13}C Metabolic MRI of the Human Heart: Initial Experience. *Circ. Res.* **2016**, *119* (11), 1177−1182.

(4) Lewis, A. J. M.; Tyler, D. J.; Rider, O. Clinical Cardiovascular Applications of Hyperpolarized Magnetic Resonance. *Cardiovasc. Drugs Ther.* **2020**, *34* (2), 231−240.

(5) Shukla-Dave, A.; Hricak, H. Role of MRI in Prostate Cancer Detection. *NMR Biomed.* **2014**, *27* (1), 16−24.

(6) Nelson, S. J.; Kurhanewicz, J.; Vigneron, D. B.; Larson, P. E. Z.; Harzstark, A. L.; Ferrone, M.; van Criekinge, M.; Chang, J. W.; Bok, R.; Park, I.; Reed, G.; Carvajal, L.; Small, E. J.; Munster, P.; Weinberg, V. K.; Ardenkjaer-Larsen, J. H.; Chen, A. P.; Hurd, R. E.; Odegardstuen, L.-I.; Robb, F. J.; Tropp, J.; Murray, J. A. Metabolic Imaging of Patients with Prostate Cancer Using Hyperpolarized [1-^{13}C]Pyruvate. *Sci. Transl. Med.* **2013**, *5* (198), 198ra108.

(7) Gallagher, F. A.; Woitek, R.; McLean, M. A.; Gill, A. B.; Manzano Garcia, R.; Provenzano, E.; Riemer, F.; Kaggie, J.; Chhabra, A.; Ursprung, S.; Grist, J. T.; Daniels, C. J.; Zaccagna, F.; Laurent, M. C.; Locke, M.; Hilborne, S.; Frary, A.; Torheim, T.; Boursnell, C.; Schiller, A.; Patterson, I.; Slough, R.; Carmo, B.; Kane, J.; Biggs, H.; Harrison, E.; Deen, S. S.; Patterson, A.; Lanz, T.; Kingsbury, Z.; Ross, M.; Basu, B.; Baird, R.; Lomas, D. J.; Sala, E.; Wason, J.; Rueda, O. M.; Chin, S. F.; Wilkinson, I. B.; Graves, M. J.; Abraham, J. E.; Gilbert, F. J.; Caldas, C.; Brindle, K. M. Imaging Breast Cancer Using Hyperpolarized Carbon-13 MRI. *Proc. Natl. Acad. Sci. U. S. A.* **2020**, *117* (4), 2092−2098.

(8) Miloushev, V. Z.; Granlund, K. L.; Boltyanskiy, R.; Lyashchenko, S. K.; DeAngelis, L. M.; Mellinghoff, I. K.; Brennan, C. W.; Tabar, V.; Yang, T. J.; Holodny, A. I.; Sosa, R. E.; Guo, Y. W. W.; Chen, A. P.; Tropp, J.; Robb, F.; Keshari, K. R. Metabolic Imaging of the Human Brain with Hyperpolarized ^{13}C Pyruvate Demonstrates 13C Lactate Production in Brain Tumor Patients. *Cancer Res.* **2018**, *78* (14), 3755−3760.

(9) Vaeggemose, M.; Schulte, R. F.; Laustsen, C. Comprehensive Literature Review of Hyperpolarized Carbon-13 MRI: The Road to Clinical Application. *Metabolites* **2021**, *11* (4), 219.

(10) Ardenkjaer-Larsen, J. H.; Boebinger, G. S.; Comment, A.; Duckett, S.; Edison, A. S.; Engelke, F.; Griesinger, C.; Griffin, R. G.; Hilty, C.; Maeda, H.; Parigi, G.; Prisner, T.; Ravera, E.; Van Bentum, J.; Vega, S.; Webb, A.; Luchinat, C.; Schwalbe, H.; Frydman, L. Facing and Overcoming Sensitivity Challenges in Biomolecular NMR Spectroscopy. *Angew. Chem., Int. Ed.* **2015**, *54* (32), 9162−9185.

(11) Nikolaou, P.; Goodson, B. M.; Chekmenev, E. Y. NMR Hyperpolarization Techniques for Biomedicine. *Chem. - Eur. J.* **2015**, *21* (8), 3156−3166.

(12) Adams, R. W.; Aguilar, J. A.; Atkinson, K. D.; Cowley, M. J.; Elliott, P. I. P. P.; Duckett, S. B.; Green, G. G. R. R.; Khazal, I. G.; Lopez-Serrano, J.; Williamson, D. C. Reversible Interactions with Para-Hydrogen Enhance NMR Sensitivity by Polarization Transfer. *Science (Washington, DC, U. S.)* **2009**, *323* (5922), 1708−1711.

(13) Iali, W.; Roy, S. S.; Tickner, B. J.; Ahwal, F.; Kennerley, A. J.; Duckett, S. B. Hyperpolarising Pyruvate through Signal Amplification by Reversible Exchange (SABRE). *Angew. Chem.* **2019**, *131* (30), 10377−10381.

(14) Tickner, B. J.; Semenova, O.; Iali, W.; Rayner, P. J.; Whitwood, A. C.; Duckett, S. B. Optimisation of Pyruvate Hyperpolarisation Using SABRE by Tuning the Active Magnetisation Transfer Catalyst. *Catal. Sci. Technol.* **2020**, *10* (5), 1343−1355.

(15) Barskiy, D. A.; Knecht, S.; Yurkovskaya, A. V.; Ivanov, K. L. SABRE: Chemical Kinetics and Spin Dynamics of the Formation of Hyperpolarization. *Prog. Nucl. Magn. Reson. Spectrosc.* **2019**, *114*−*115*, 33−70.

(16) Barskiy, D. A.; Shchepin, R. V.; Tanner, C. P. N.; Colell, J. F. P.; Goodson, B. M.; Theis, T.; Warren, W. S.; Chekmenev, E. Y. The Absence of Quadrupolar Nuclei Facilitates Efficient ^{13}C Hyper-

polarization via Reversible Exchange with Parahydrogen. *ChemPhysChem* **2017**, *18* (12), 1493−1498.
(17) Truong, M. L.; Theis, T.; Coffey, A. M.; Shchepin, R. V.; Waddell, K. W.; Shi, F.; Goodson, B. M.; Warren, W. S.; Chekmenev, E. Y. ^{15}N Hyperpolarization by Reversible Exchange Using SABRE-SHEATH. *J. Phys. Chem. C* **2015**, *119* (16), 8786−8797.
(18) Theis, T.; Truong, M. L.; Coffey, A. M.; Shchepin, R. V.; Waddell, K. W.; Shi, F.; Goodson, B. M.; Warren, W. S.; Chekmenev, E. Y. Microtesla SABRE Enables 10% Nitrogen-15 Nuclear Spin Polarization. *J. Am. Chem. Soc.* **2015**, *137* (4), 1404−1407.
(19) Shchepin, R. V.; Birchall, J. R.; Chukanov, N. V.; Kovtunov, K. V.; Koptyug, I. V.; Theis, T.; Warren, W. S.; Gelovani, J. G.; Goodson, B. M.; Shokouhi, S.; Rosen, M. S.; Yen, Y.; Pham, W.; Chekmenev, E. Y. Hyperpolarizing Concentrated Metronidazole $^{15}NO_2$ Group over Six Chemical Bonds with More than 15% Polarization and a 20 minute Lifetime. *Chem. - Eur. J.* **2019**, *25* (37), 8829−8836.
(20) Knecht, S.; Blanchard, J. W.; Barskiy, D.; Cavallari, E.; Dagys, L.; van Dyke, E.; Tsukanov, M.; Bliemel, B.; Münnemann, K.; Aime, S.; Reineri, F.; Levitt, M. H.; Buntkowsky, G.; Pines, A.; Blümler, P.; Budker, D.; Eills, J. Rapid Hyperpolarization and Purification of the Metabolite Fumarate in Aqueous Solution. *Proc. Natl. Acad. Sci. U. S. A.* **2021**, *118* (13), e2025383118.
(21) Kovtunov, K. V.; Pokochueva, E. V.; Salnikov, O. G.; Cousin, S. F.; Kurzbach, D.; Vuichoud, B.; Jannin, S.; Chekmenev, E. Y.; Goodson, B. M.; Barskiy, D. A.; Koptyug, I. V. Hyperpolarized NMR Spectroscopy: D-DNP, PHIP, and SABRE Techniques. *Chem. - Asian J.* **2018**, *13* (15), 1857−1871.
(22) Cavallari, E.; Carrera, C.; Sorge, M.; Bonne, G.; Muchir, A.; Aime, S.; Reineri, F. The ^{13}C Hyperpolarized Pyruvate Generated by ParaHydrogen Detects the Response of the Heart to Altered Metabolism in Real Time. *Sci. Rep.* **2018**, *8* (1), 8366.
(23) Cavallari, E.; Carrera, C.; Aime, S.; Reineri, F. ^{13}C MR Hyperpolarization of Lactate by Using ParaHydrogen and Metabolic Transformation in Vitro. *Chem. - Eur. J.* **2017**, *23* (5), 1200−1204.
(24) Cavallari, E.; Carrera, C.; Aime, S.; Reineri, F. Studies to Enhance the Hyperpolarization Level in PHIP-SAH-Produced C13-Pyruvate. *J. Magn. Reson.* **2018**, *289*, 12−17.
(25) Chapman, B.; Joalland, B.; Meersman, C.; Ettedgui, J.; Swenson, R. E.; Krishna, M. C.; Nikolaou, P.; Kovtunov, K. V.; Salnikov, O. G.; Koptyug, I. V.; Gemeinhardt, M. E.; Goodson, B. M.; Shchepin, R. V.; Chekmenev, E. Y. Low-Cost High-Pressure Clinical-Scale 50% Parahydrogen Generator Using Liquid Nitrogen at 77 K. *Anal. Chem.* **2021**, *93* (24), 8476−8483.
(26) TomHon, P.; Akeroyd, E.; Lehmkuhl, S.; Chekmenev, E. Y.; Theis, T. Automated Pneumatic Shuttle for Magnetic Field Cycling and Parahydrogen Hyperpolarized Multidimensional NMR. *J. Magn. Reson.* **2020**, *312*, 106700.
(27) Theis, T.; Truong, M. L.; Coffey, A. M.; Shchepin, R. V.; Waddell, K. W.; Shi, F.; Goodson, B. M.; Warren, W. S.; Chekmenev, E. Y. Microtesla SABRE Enables 10% Nitrogen-15 Nuclear Spin Polarization. *J. Am. Chem. Soc.* **2015**, *137* (4), 1404−1407.
(28) Colell, J. F. P.; Logan, A. W. J.; Zhou, Z.; Shchepin, R. V.; Barskiy, D. A.; Ortiz, G. X.; Wang, Q.; Malcolmson, S. J.; Chekmenev, E. Y.; Warren, W. S.; Theis, T. Generalizing, Extending, and Maximizing Nitrogen-15 Hyperpolarization Induced by Parahydrogen in Reversible Exchange. *J. Phys. Chem. C* **2017**, *121* (12), 6626−6634.
(29) Hermkens, N. K. J.; Feiters, M. C.; Rutjes, F. P. J. T.; Wijmenga, S. S.; Tessari, M. High Field Hyperpolarization-EXSY Experiment for Fast Determination of Dissociation Rates in SABRE Complexes. *J. Magn. Reson.* **2017**, *276* (2017), 122−127.
(30) Kidd, B. E.; Gesiorski, J. L.; Gemeinhardt, M. E.; Shchepin, R. V.; Kovtunov, K. V.; Koptyug, I. V.; Chekmenev, E. Y.; Goodson, B. M. Facile Removal of Homogeneous SABRE Catalysts for Purifying Hyperpolarized Metronidazole, a Potential Hypoxia Sensor. *J. Phys. Chem. C* **2018**, *122* (29), 16848−16852.
(31) Iali, W.; Olaru, A. M.; Green, G. G. R.; Duckett, S. B. Achieving High Levels of NMR-Hyperpolarization in Aqueous Media With Minimal Catalyst Contamination Using SABRE. *Chem. - Eur. J.* **2017**, *23* (44), 10491−10495.

https://doi.org/10.1021/jacs.1c09581
J. Am. Chem. Soc. 2022, 144, 282−287